PAPER

The role of oxygenated species in the catalytic self-coupling of MeOH on O pre-covered Au(111)

R. Réocreux, [ID] [a] I. Fampiou [ID] [b] and M. Stamatakis [ID] *[a]

The oxidation of alcohols plays a central role in the valorisation of biomass, in particular when performed with a non-toxic oxidant such as O_2. Aerobic oxidation of methanol on gold has attracted attention lately and the main steps of its mechanism have been described experimentally. However, the exact role of O and OH on each elementary step and the effect of the interactions between adsorbates are still not completely understood. Here we investigate the mechanism of methanol oxidation to $HCOOCH_3$ and CO_2. We use Density Functional Theory (DFT) to assess the energetics of the underlying pathways, and subsequently build lattice kinetic Monte Carlo (kMC) models of increasing complexity, to elucidate the role of different oxygenates. Detailed comparisons of our simulation results with experimental temperature programmed desorption (TPD) spectra enable us to validate the mechanism and identify rate determining steps. Crucially, taking into account dispersion (van der Waals forces) and adsorbate–adsorbate lateral interactions are both important for reproducing the experimental data.

Introduction

The oxidation of alcohols is a well-established method to obtain a wide variety of organic compounds with oxidation states ranging from −II (methanol) to +IV (CO_2). Albeit very versatile in that regard, the oxidation of alcohols nonetheless requires the development of complex oxidative agents[1] or catalysts[2,3] in order to avoid the combustion route and obtain compounds with the desired oxidation states (*e.g.* carbonyls, acids or esters).[4] Heterogeneous catalysis can provide a means for selective alcohol oxidations, especially in the context of biomass valorisation, whereby atom economy and ease of product separation are key. Here, we shall only focus on the oxidation of alcohols to carboxylic acids and esters (oxidation state +II) of energetic and industrial relevance.

[a]Thomas Young Centre and Department of Chemical Engineering, University College London, Roberts Building, Torrington Place, London, WC1E 7JE, UK. E-mail: m.stamatakis@ucl.ac.uk

[b]Department of Chemistry and Chemical Biology, Harvard University, Cambridge, Massachusetts 02138, USA

Among the mildest heterogeneous catalysts, platinum group metals (Pt, Pd) exhibit appreciable conversions for aerobic oxidation in water to carboxylic acids.[5] The ability of these metals to activate O_2 is essential to their activity.[6] However, the undesired consequence of such a property is self-oxidation, which leads to metal oxides, thereby impacting the activity of the catalyst.[7] Selectivity issues exist as well, since platinum group metals can also yield decomposition products *via* C–C cleavages, as well as CO_2 and water *via* over-oxidation.[5,8] On the other hand, gold, as the noblest metal, remains metallic under oxidative conditions. Although the splitting of O_2 on pure gold is highly activated in the gas phase or in neutral aqueous media, it becomes more facile under basic conditions,[9] and as a matter of fact, gold is one of the most effective catalysts for the oxidation of alcohols to carboxylates when used under basic conditions.[5]

Selective alcohol oxidation in the gas phase over gold catalysts has also been achieved. Of particular interest for our work is the oxidation of methanol to methyl formate using O_2 as an oxidant on a nanoporous silver-doped gold $Ag_\varepsilon Au_{1-\varepsilon}$ catalyst ($\varepsilon = 0.01–0.03$).[10] The silver sites activate O_2 without the use of water or a base and initiate the oxidation cascade, the mechanism of which has been progressively elucidated over the last three decades. In the late 80s, the pioneering work by Madix and co-workers showed that surface oxygen adatoms on coinage metals (Cu, Ag, Au) have Brønsted and Lewis basic properties and can be used to perform X–H cleavages (X = C, N, O, S).[11–13] Reacting methanol on O pre-covered gold surfaces yields different products, namely, formaldehyde (CH_2O), hydrogen (H_2), water (H_2O), carbon dioxide (CO_2), and methyl formate ($HCOOCH_3$).[13–15] Experimental mechanistic investigations have provided a description of the main features of the overall mechanism (see Fig. 1). For instance, vibrational spectroscopy has showed that adsorbed methanol (when dosed above 150 K) reacts quantitatively with the O adatoms to form CH_3O (methoxy).[15] After a first C–H activation (potentially assisted by O, OH or another CH_3O),[14,15] CH_2O (formaldehyde) is formed and can readily associate with the remaining amount of either CH_3O or O, yielding H_2COOCH_3 (hemiacetal alkoxide) and H_2COO (methanediolate), respectively. Further C–H activations produce $HCOOCH_3$ (methyl formate, the coupling product) and CO_2 (over-
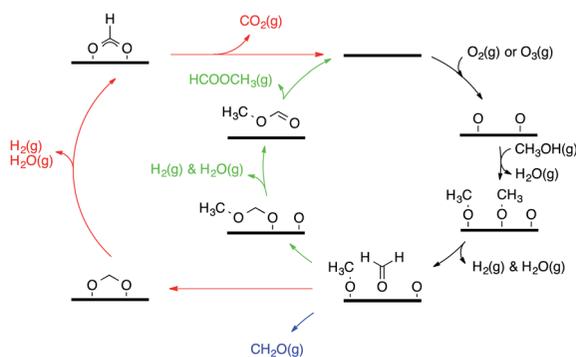

Fig. 1 General mechanism for methanol oxidation over gold (represented as a thick horizontal line). The green arrows highlight the coupling while the red ones highlight the over-oxidation route.

oxidation product), which both desorb. Among the sequence of steps involved in the formation of the coupling product, H/D isotopic substitutions have showed that the desorption of $HCOOCH_3$ is limited by the C–H activation step from CH_3O.[15] Moreover, $^{16}O/^{18}O$ substitution shows that the nucleophilic addition of O onto CH_2O to H_2COO is reversible.[16] Other molecules desorb, such as H_2O (essentially resulting from O deprotonation of CH_3OH into CH_3O by O), CH_3OH (re-hydrogenation of CH_3O from aliphatic hydrogen) and unreacted CH_2O.

This understanding of the main features of the mechanism has paved the way for the successful extension of this chemistry to other alcohols (aliphatic alcohols,[16–18] allylic alcohol[19]), aldehydes,[20] and nucleophiles (amines).[21] Remarkably, this mechanism translates to catalytic systems employing nanoporous gold as a catalyst (moderate temperatures and ambient pressures).[10,22,23] Reece *et al.* have recently proved this transferability of the kinetic parameters of a set of elementary steps from surface science to catalysis, showing narrow pressure and material gaps.[24,25] Even if the main features of the mechanism have been described, several aspects are still elusive to experiments, *i.e.* the precise role of O, OH and CH_3O as bases and the details of the over-oxidation route (for instance how formate gets deprotonated).

Previous theoretical studies based on Density Functional Theory (DFT) have also shed light on the role of the different species on Au(111) under UHV conditions. The early work by Xu *et al.*[16,26] substantiated the experimental mechanism by computing the reaction and activation energies of the main elementary steps. Comparing both the coupling and over-oxidation routes, Liu *et al.*[27] provided qualitative insight into the influence of the coverage of oxygen adatoms on the selectivity of the catalyst. Yet, the role of OH was not investigated. Wang *et al.*[28] studied the over-oxidation reactions extensively (neglecting the coupling route) and proposed different mechanisms under kinetic and thermodynamic controls. In spite of the significance of these early studies, van der Waals corrections were not common at the time and were therefore not included in their work. More recent work by Kabeer *et al.*[29] has showed that vdW interactions are critical to describe the interaction of alkoxides on gold surfaces. Moreover, the complexity of the reaction network (wide and branched) requires a kinetic analysis to bridge the gap between molecular properties (such as activation/reaction energies) and macroscopic behaviours. Such an analysis can be achieved using the energetic span model introduced by Kozuch and Shaik,[30–32] which can be generalised to the understanding of Temperature Programmed Desorption/Reaction (TPD/TPR) experiments.[33]

However, to understand in detail non-steady state behaviours, pressure/coverage effects, or the relative contribution of one mechanistic pathway *versus* another, kinetic simulations become necessary. Such simulations constitute a valuable tool for the analysis of complex reaction networks obtained from DFT calculations, especially when the energetic landscapes of different pathways are close, indicating a tendency for competition.[34] Kinetic simulations can be performed within two different formalisms, either using mean-field deterministic equations or performing stochastic (Monte-Carlo) simulations. The former neglects spatial correlations and "averages out" the effect of lateral interactions, whereas the latter describes each adsorbate individually (as an entity occupying a specific site), and explicitly accounts for correlation. In spite of its computational cost (which is still negligible compared to the DFT mechanistic inspection),

the stochastic approach allows for a detailed description of interactions between species, and provides insight into the influence of clustering/surface exclusion on the kinetics of a mechanism.[35–37]

Here we study the Temperature Programmed Oxidation (TPO) of methanol to methyl formate on the O pre-covered Au(111) surface. To understand the exact role of the different oxygenates under reacting conditions, we first re-examine the mechanism including weak van der Waals interactions. We carefully consider both the coupling route and one possible over-oxidation pathway previously described in the literature. Additionally, we have performed DFT-parameterised kinetic Monte-Carlo (kMC) simulations of the TPO spectra, which reproduce and rationalise the experimental observations. This multi-scale approach provides a dynamic description of the catalytic surface under reaction conditions and allows for the identification of the role of each species present on the surface during the course of the oxidation.

Computational details

Our approach relies on two theories. On the one hand, we determine the mechanism and its energetics at the atomistic level using *ab initio* calculations (DFT). On the other hand, this enables the calculation of rate constants from transition state theory (TST), and the subsequent parameterisation of a kMC model, which captures the chemistry at the catalyst level.

Density function theory calculations

All the atomistic simulations were performed using periodic DFT as implemented in the Vienna *Ab initio* Simulation Package (version 5.4).[38–40] The electronic exchange and correlation potential was modelled using the PBE-TS functional,[41] which accounts for weak dispersion interactions between atomic structures. The core electrons were treated using the Projected Augmented Wave (PAW)[42] method and the valence electronic density was expanded on a plane wave basis set with an energy cut-off of 400 eV. When solving the Kohn–Sham equations, the electronic density was optimised until the associated energy reaches the threshold of 10^{-6} eV.

In all of our DFT calculations we focused on the Au(111) surface. We used a lattice constant of 4.162 Å, which was obtained by minimising the energy the FCC unit cell of Au. The system was described using a unit cell containing a 4 layer p(4 × 4) slab and 23 Å of vacuum, in order to avoid the interaction between two periodic images along the coordinate perpendicular to the slab. The atoms of the two lower layers were fixed at their bulk positions, relaxing the coordinates of all the other atoms of the periodic cell, until forces drop below 0.02 eV Å^{-1}. The Brillouin zone was sampled using a 7 × 7 × 1 Monkhorst–Pack k-point mesh.[43]

Stable intermediates were located using the Conjugate Gradient algorithm. Transition states were first approached using the climbing image Nudge Elastic Band method,[44,45] before switching to Dimer[46,47] and/or Quasi-Newton algorithms. All structures were characterised by running vibrational analyses, checking in particular that transition states are indeed first-order saddles, containing exactly one imaginary frequency.

Each elementary step is energetically characterised by the reaction energies ($\Delta_r E$ and $\Delta_r E_\infty$), the forward and reverse activation energies ($\Delta^\ddagger E_{fwd}$ and $\Delta^\ddagger E_{rev}$)
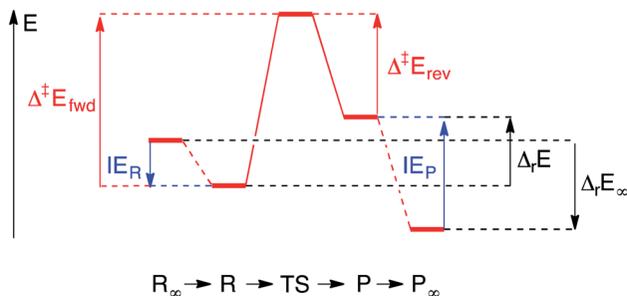
Fig. 2 Energy diagram of the elementary process going from the reactant state R to the product state P *via* the transition state (TS). The states of infinite separation of the reactants (R_∞) and the products (P_∞) are also indicated. In this example, there are attractive interactions between the reactant molecules and repulsive interactions between the products.

and the interaction energies of the reactants (IE_R) and the products (IE_P), which are defined in Fig. 2. To take into account the thermodynamic barrier that needs to be overcome in order to bring the reactants together in the ready-to-react configuration, we further define the apparent forward and reverse activation energies as follows:

$$\overline{\Delta^{\ddagger}E_{fwd}} = \max\left(\Delta^{\ddagger}E_{fwd}, \ \Delta^{\ddagger}E_{fwd} + IE_R\right) \tag{i}$$

$$\overline{\Delta^{\ddagger}E_{rev}} = \max\left(\Delta^{\ddagger}E_{rev}, \ \Delta^{\ddagger}E_{rev} + IE_P\right) \tag{ii}$$

Graph-theoretical kinetic Monte-Carlo simulations

The simulations were performed with the graph-theoretical kinetic Monte-Carlo framework as implemented in software *Zacros* (version 2.0) developed by Stamatakis and co-workers.[48,49] Each event is described using a forward rate constant k_{fwd} from state R to state P (representing the reactants and the products, respectively) and a reverse rate constant k_{rev} from state P to state R. They can be computed from DFT and TST as follows:

$$k_{fwd}(T) = \frac{k_B T}{h} \frac{Q^{\ddagger}(T)}{Q_R(T)} \exp\left(-\frac{\Delta^{\ddagger}E_{fwd}}{k_B T}\right) \tag{iii}$$

$$k_{rev}(T) = \frac{k_B T}{h} \frac{Q^{\ddagger}(T)}{Q_P(T)} \exp\left(-\frac{\Delta^{\ddagger}E_{rev}}{k_B T}\right) \tag{iv}$$

$$\Delta^{\ddagger}E_{fwd} - \Delta^{\ddagger}E_{rev} = \Delta_r E \tag{v}$$

where $\Delta^{\ddagger}E_{fwd}$ and $\Delta^{\ddagger}E_{rev}$ are the DFT-computed activation energies of the forward and reverse elementary steps, and Q_R, $Q^{\ddagger}$ and Q_P the temperature dependent partition functions of the reactant(s), transition state and product(s) respectively. They include translational, rotational and vibrational components, as appropriate. The vibrational partition functions are evaluated within the harmonic approximation (with DFT-computed vibrational frequencies), taking the bottom of the

potential well as the zero energy level. Thus, no zero-point energy correction is needed for the activation energies. For gas phase species only, we employ the high-temperature approximation of the rigid rotor and the partition function of the free translator, for the respective degrees of freedom. This approach, recently compared to state-of-the-art molecular dynamics, gives a reasonable description of the free energy landscape of desorption from metal surfaces.[50]

For our kMC simulations of methanol oxidative coupling on Au(111), different scenarios were considered. They consist of a different initial state (chemical composition) and a different sub-set of elementary steps as described in the results section. Simulations are performed with or without lateral interactions, that is taking into account or neglecting the IE_R or IE_P for each elementary step. In the former case, appropriate energetic interactions terms are included in a cluster expansion Hamiltonian and the activation energies are computed via Brønsted–Evans–Polanyi relations, as per the previously published approach.[49] For each scenario, 10 kMC simulations are performed and averaged to give the final TPO spectra. The simulations are run on a periodic lattice, which consists of 15 300 sites: 5100 top sites and 10 200 three-fold sites (fcc/hcp treated as one site type). The coverages are reported in units of a monolayer (ML), defined as the number of adsorbates on the surface normalised with respect to the number of top sites.

Results and discussion

DFT results

Since we aim at modelling TPD experiments where desorption plays a key role, it is very important to estimate the adsorption energies accurately. Previous studies investigating the oxidation of methanol on O-precovered Au(111) used Generalised Gradient Approximation (GGA) functionals with no corrections for dispersion interactions. As shown in Table 1, these functionals (PW91 and PBE) greatly underestimate the adsorption of closed-shell adsorbates on Au(111). When adding the Tkatchenko–Scheffler correction for vdW interactions, the adsorption energies become closer to the experimental values available in the literature.

After thus validating the PBE-TS functional, we turned our attention to the reaction network of methanol oxidation on O-precovered Au(111), and performed DFT calculations to elucidate the underlying elementary steps (Table 2). For each step, we report all the energies appearing in Fig. 2 and eqn (i) and (ii). The elementary steps are grouped into different types. The first one corresponds to the desorption processes. Most of the species show low (CO_2 and H_2) to moderate (CH_2O, CH_3OH, H_2O, $HCOOCH_3$) affinities to Au(111). Only the associative adsorption of H_2 has been considered as an activated process, as it involves bond cleavage. The activation energy thereof ($\Delta^{\ddagger}E_{fwd} = 0.68$ eV) is comparable to other

Table 1 Comparison between experimental and DFT adsorption energies for three major compounds of the TPO of methanol to methyl formate on Au(111)

E_{ads} (eV)	PW91 (Liu)[27]	PBE (Wang)[28]	PBE-TS (this work)	Experimental
CH_3OH	−0.09	−0.17	−0.44	−0.42 ± 0.02 (ref. 14)
CH_2O	−0.09	−0.11	−0.32	−0.32 ± 0.03 (ref. 51)
$HCOOCH_3$	−0.02	—	−0.42	−0.54 (ref. 25)

Table 2 Elementary steps of the self-coupling of methanol to methyl formate on O pre-covered Au(111) surface. The forward and reverse activation energies ($\Delta^{\ddagger}E_{fwd}$ and $\Delta^{\ddagger}E_{rev}$), the reaction energy ($\Delta_{r}E$), and the infinite separation reaction energy ($\Delta_{r}E_{\infty}$) are defined in Fig. 2. The forward and reverse activation energies ($\Delta^{\ddagger}E_{fwd}$ and $\Delta^{\ddagger}E_{rev}$) are defined in the Methods section. $\overline{\Delta^{\ddagger}E_{fwd}}$ and $\overline{\Delta^{\ddagger}E_{rev}}$ are the apparent activation energies as defined in Fig. 2. The energies are given in eV and do not include zero-point energy corrections

	Reaction number	Reaction	$\Delta^{\ddagger}E_{fwd}$	$\Delta^{\ddagger}E_{rev}$	$\Delta_{r}E$	IE_{R}	IE_{P}	$\overline{\Delta^{\ddagger}E_{fwd}}$	$\overline{\Delta^{\ddagger}E_{rev}}$	$\Delta_{r}E_{\infty}$
Desorption	R1	$CH_3OH \rightarrow CH_3OH(g)$	0.44	0.00	0.44	—	—	0.44	0.00	0.44
	R2	$CH_2O \rightarrow CH_2O(g)$	0.32	0.00	0.32	—	—	0.32	0.00	0.32
	R3	$HCOOCH_3 \rightarrow HCOOCH_3(g)$	0.42	0.00	0.42	—	—	0.42	0.00	0.42
	R4	$CO_2 \rightarrow CO_2(g)$	0.21	0.00	0.21	—	—	0.21	0.00	0.21
	R5	$H + H \rightarrow H_2(g)$	0.66	0.64	0.02	0.02	—	0.68	0.64	0.04
	R6	$H_2O \rightarrow H_2O(g)$	0.30	0.00	0.30	—	—	0.30	0.00	0.30
CH_3OH/CH_3O	R7	$CH_3OH \rightarrow CH_3O + H$	1.70	0.53	1.17	—	0.06	1.70	0.59	1.11
	R8	$CH_3OH + O \rightarrow CH_3O + OH$	0.26	0.26	0.00	-0.24	-0.10	0.26	0.26	-0.14
	R9	$CH_3OH + OH \rightarrow CH_3O + H_2O$	0.03	0.00	0.03	-0.26	-0.15	0.03	0.00	-0.08
CH_3O/CH_2O	R10	$CH_3O \rightarrow CH_2O + H$	0.76	0.41	0.35	—	0.06	0.76	0.46	0.29
	R11	$CH_3O + O \rightarrow CH_2O + OH$	0.43	1.55	-1.12	0.13	-0.03	0.56	1.55	-0.96
	R12	$CH_3O + OH \rightarrow CH_2O + H_2O$	0.70	1.91	-1.21	0.09	-0.25	0.79	1.91	-0.88
	R13	$CH_3O + CH_3O \rightarrow CH_3OH + CH_2O$	0.66	1.79	-1.14	0.15	-0.17	0.81	1.79	-0.82
A_N2	R14	$CH_2O + CH_3O \rightarrow H_2COOCH_3$	0.24	0.83	-0.59	0.01	—	0.25	0.83	-0.58
	R15	$CH_2O + O \rightarrow H_2COO$	0.10	0.54	-0.43	-0.14	—	0.10	0.54	-0.57
	R16	$CH_2O + OH \rightarrow H_2COOH$	0.06	0.61	-0.56	-0.03	—	0.06	0.61	-0.58
$H_2COOCH_3/HCOOCH_3$	R17	$H_2COOCH_3 \rightarrow HCOOCH_3 + H$	0.53	1.19	-0.66	—	0.00	0.53	1.19	-0.65
	R18	$H_2COOCH_3 + O \rightarrow HCOOCH_3 + OH$	0.23	2.36	-2.13	0.15	-0.07	0.38	2.36	-1.91
	R19	$H_2COOCH_3 + OH \rightarrow HCOOCH_3 + H_2O$	0.71	2.63	-1.92	-0.08	-0.18	0.71	2.63	-1.82
$H_2COO/HCOO$	R20	$H_2COO \rightarrow HCOO + H$	0.28	1.34	-1.06	—	0.31	0.28	1.65	-1.37

Table 2 (Contd.)

Reaction number	Reaction	$\Delta^\ddagger E_{fwd}$	$\Delta^\ddagger E_{rev}$	$\Delta_r E$	IE_R	IE_P	$\overline{\Delta^\ddagger E_{fwd}}$	$\overline{\Delta^\ddagger E_{rev}}$	$\Delta_r E_\infty$
R21	$H_2COO + O \rightarrow HCOO + OH$	0.12	3.00	−2.87	0.22	−0.03	0.34	3.00	−2.62
R22	$H_2COO + OH \rightarrow HCOO + H_2O$	0.20	3.16	−2.96	0.14	−0.28	0.34	3.16	−2.54
HCOO/CO$_2$									
R23	$x^2\text{-HCOO} \rightarrow x^1\text{-HCOO}$	0.78	0.13	0.65	—	—	0.78	0.13	0.65
R24	$x^1\text{-HCOO} \rightarrow H + CO_2(g)$	0.05	0.99	−0.94	—	—	0.05	0.99	−0.94
R25	$x^2\text{-HCOO} + O \rightarrow OH + CO_2(g)$	0.94	2.49	−1.55	0.01	—	0.94	2.49	−1.54
R26	$x^2\text{-HCOO} + OH \rightarrow H_2O + CO_2(g)$	1.18	2.60	−1.43	−0.03	—	1.18	2.60	−1.46
Water chemistry									
R27	$H_2O \rightarrow H + OH$	1.80	0.56	1.24	—	0.07	1.80	0.63	1.17
R28	$OH \rightarrow O + H$	1.96	0.60	1.36	—	0.11	1.96	0.71	1.26
R29	$OH + OH \rightarrow H_2O + O$	0.05	0.29	−0.24	0.11	−0.21	0.17	0.29	0.09

DFT studies,[52] which surprisingly over-estimate the experimental barrier of 0.28 eV associated with a desorption peak at 110 K.[53] At such a low temperature however, quantum tunnelling of the nuclei might dominate. This has for example been described for PdCu(111) single-atom alloys, on which a similar barrier of 0.65 eV for the associative desorption of H_2 without tunnelling is decreased down to approximately 0.3 eV when treating nuclear quantum effects properly.[54]

Upon adsorption of CH_3OH, the first key step is the formation of the methoxy CH_3O intermediate. Without the help of a base, the O–H cleavage is extremely endothermic ($\Delta_r E > 1$ eV) and more difficult than the desorption of CH_3OH ($\Delta_r E = 0.44$ eV). This is consistent with the experimental observation that, when adsorbed on Au(111), methanol desorbs at a low temperature without reacting.[14] The addition of surface O or OH dramatically lowers the kinetic barrier of this O–H cleavage and makes the production of the co-adsorbed configuration ($CH_3O + OH$ or $CH_3O + H_2O$) athermic. When considering the diffusion of the species, the overall acid/base reaction becomes slightly exothermic ($\Delta_r E_\infty \sim -0.1$ eV). Because of the significance of the role of O/OH to opening new routes, we have investigated their influence on the various subsequent C–H cleavages.

The C–H cleavage of CH_3O to CH_2O is moderately activated and can happen on its own ($\overline{\Delta^\ddagger E_{fwd}} = 0.76$ eV, without zero-point energy corrections). O lowers the apparent activation energy to 0.56 eV whereas OH increases it to 0.79 eV. The same trend is seen for the C–H cleavage from the coupling product H_2COOCH_3 to methyl formate $HCOOCH_3$. On the CO_2 route however, O and OH do not offer preferred alternative pathways for the C–H cleavage of H_2COO to HCOO and HCOO to CO_2. Concerning the latter step, it is worth noting that formate HCOO needs to go through a configurational change from bidentate $\varkappa^2$-HCOO to monodentate $\varkappa^1$-HCOO to be able to dehydrogenate. The actual rate-limiting step is this configurational change ($\overline{\Delta^\ddagger E_{fwd}} = 0.78$ eV) while the C–H cleavage from the monodentate configuration happens with almost no barrier ($\overline{\Delta^\ddagger E_{fwd}} = 0.05$ eV). Similar $\varkappa^1/\varkappa^2$ configurational equilibrium has been reported on different metals,[55,56] e.g. on Pt(111) monodentate $\varkappa^1$-HCOO is also less stable and also more reactive towards C–H activation.[56]

The compounds with higher oxidation states ($HCOOCH_3$ and HCOO) are obtained from the coupling of formaldehyde (an electrophile) with O, OH or CH_3O, which are nucleophiles on top of their aforementioned reactivity as Brønsted bases. For each nucleophile, the coupling reaction is exothermic ($\Delta_r E_\infty \sim -0.6$ eV). The structures of the three transition states are given in Fig. 3. The highest barrier is found for the coupling of CH_2O with methoxy CH_3O and is associated with an earlier transition state, as evidenced by the C···O distance in the transition state (see Fig. 3). O and OH, as less bulky nucleophiles, exhibit lower activation energies. Even if OH
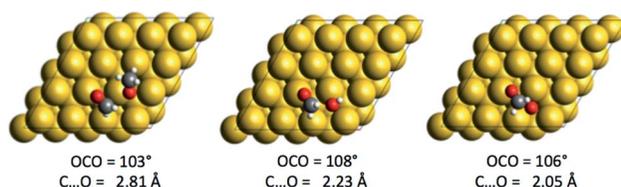

OCO = 103°   OCO = 108°   OCO = 106°
C...O = 2.81 Å   C...O = 2.23 Å   C...O = 2.05 Å

Fig. 3 Structures of the three transition states associated with the A_N2 of O, OH and CH_3O onto CH_2O.

seems to be the most reactive species, experimental studies suggest that OH is either only transient (with an undetectable surface concentration) or more strongly solvated with water molecules.[57] It is therefore likely that the coupling with OH is more complicated than described here and could involve more steps (de-coordinating water from OH to make it reactive), or it could be that it just never happens.

Because of the extensive branched reaction network underpinning this system, we need kinetic analysis to be able to assess how the proposed mechanism performs, and to explain macroscopic behaviours. Intuitively, we would not expect any methyl formate to be formed on the surface since the coupling of formaldehyde with O (and OH) is less activated ($\overline{\Delta^{\ddagger}E_{fwd}} < 0.10$ eV) than with methoxy CH_3O ($\overline{\Delta^{\ddagger}E_{fwd}} = 0.25$ eV). However, this is without considering the entropic contribution of the transition state, which is very loose for the coupling with CH_3O and tighter for the coupling with O (see the variation of the C–O distances, from 2.03 Å to 2.81 Å, in the transition states in Fig. 3). Moreover the usual approximation of considering the diffusion of surface species as faster than all other steps is not valid for O ($\overline{\Delta^{\ddagger}E_{fwd}} = 0.50$ eV). kMC simulations are thus needed for capturing such complexities and describing these effects properly. For the purpose of analysis, we have considered three scenarios in our kMC simulations, focusing on different sets of elementary steps, and starting the system from different initial states. For each scenario, the kMC simulations have been performed twice: with and without the lateral interactions involved in the reactant and product states.

First scenario: the chemistry of methoxy only

In the first scenario, the initial state considers only CH_3O on the surface. This corresponds to the assumption that the deposited CH_3OH molecules have quantitatively reacted with surface O to produce H_2O (assumed to desorb as soon as it is formed) and CH_3O. The simulations are therefore initiated with 0.01 ML or CH_3O on the surface and only take into account the steps that do not involve O or OH (*i.e.* R1, R2, R3, R5, R7, R10, R13, R14 and R17). The associated TPDs are given in Fig. 4. Hydrogen desorbs at 274 K, while $HCOOCH_3$, CH_3OH and CH_2O desorb almost simultaneously at around 210 K. The analysis of the surface species shows that, from this temperature, significant amounts of CH_3O are converted to CH_2O. The reaction is therefore limited by the C–H activation step from CH_3O to CH_2O, in accordance with experimental evidence based on the kinetic isotope effect.[15] In spite of the simplifications, this scenario already reproduces the desorption peaks of these molecules well, with a deviation compared to the experiments of about 30 K. Since OH_x ($x = 0, 1, 2$) are not explicitly taken into account (only implicitly *via* the presence of CH_3O that can only be produced with OH_x), we do not see water and CO_2 coming off the surface. It is worth noting here that the lateral interactions do not exert a strong influence on position of the peak in this scenario (as shown in Fig. 4).

Second and third scenarios: the chemistry of methoxy in presence of oxygen adatoms

In the second scenario, we have added 0.02 ML of O. This should in principle open various reactive routes. To progressively build on the complexity of the reaction network, we have first considered only the elementary steps associated with the successive recombination of H with O and OH to form water (R27, R28
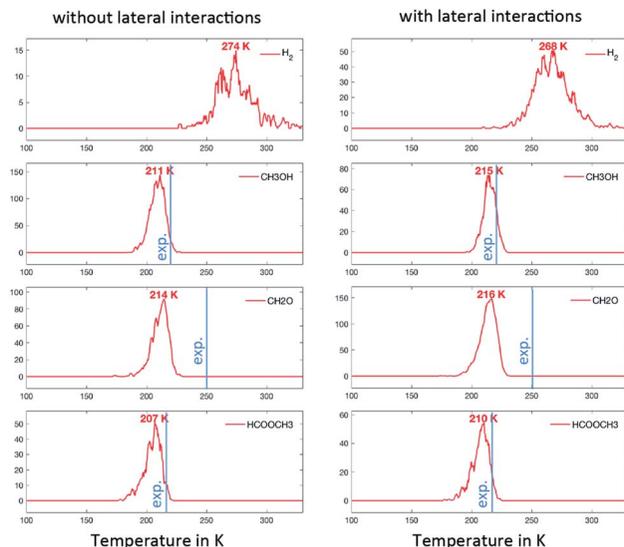
Fig. 4 TPO spectra of methanol on Au(111) for scenario #1. The temperature ramp is 10 K s^{-1}. The initial coverage in CH$_3$O is 0.1 ML. The blue line corresponds to the approximate position of the experimental peak.

and R29) and the reactions of the over-oxidation route (R15, R20, R23 and R24), in addition to the steps of the first scenario. This set of elementary steps is closely related to that chosen by Reece *et al.* in their kinetic model based on experimental kinetic parameters.[25] The two-step C–H cleavage of formate (HCOO) into CO$_2$ (configurational change and C–H scission) is modelled as a single elementary step, using the kinetic parameters of the configurational change (which is rate determining). The corresponding TPDs are given in Fig. 5. When lateral interactions are neglected, we see, in addition to the peaks discussed above, a peak for CO$_2$ at ∼260 K and a peak for H$_2$O at ∼280 K. These two peaks are seen experimentally, although, in the case of water, the major peak is still not reproduced with our simulations. When adding the lateral interactions, most surface oxygen reacts with formaldehyde to ultimately produce CO$_2$, yielding a noisier spectrum for water (as less water desorbs) and a more defined spectrum for CO$_2$. This results from the strong attractive interaction between CH$_2$O with O (−0.14 eV) that dramatically increases the probability that they meet (especially at low temperature). Although there is experimental evidence of water desorbing concomitantly with CO$_2$ around 275 K, the main desorption peak is seen around 220 K. O must therefore be involved in protonation/deprotonation steps at an early stage of the simulation.

To address this problem, in our last scenario (Fig. 6), we have considered the same set of elementary steps and have added the C–H activation steps that become easier in the presence of O (*i.e.* CH$_3$O + O = CH$_2$O + OH and H$_2$COOCH$_3$ + O = HCOOCH$_3$ + OH, referred to as R11 and R18 in Table 2). The production of CH$_2$O, CH$_3$OH and H$_2$ remains essentially comparable with the previous simulations and agrees well with experimental observations. Interestingly, the desorption of HCOOCH$_3$ now appears as bimodal (Fig. 6, left panel). The first
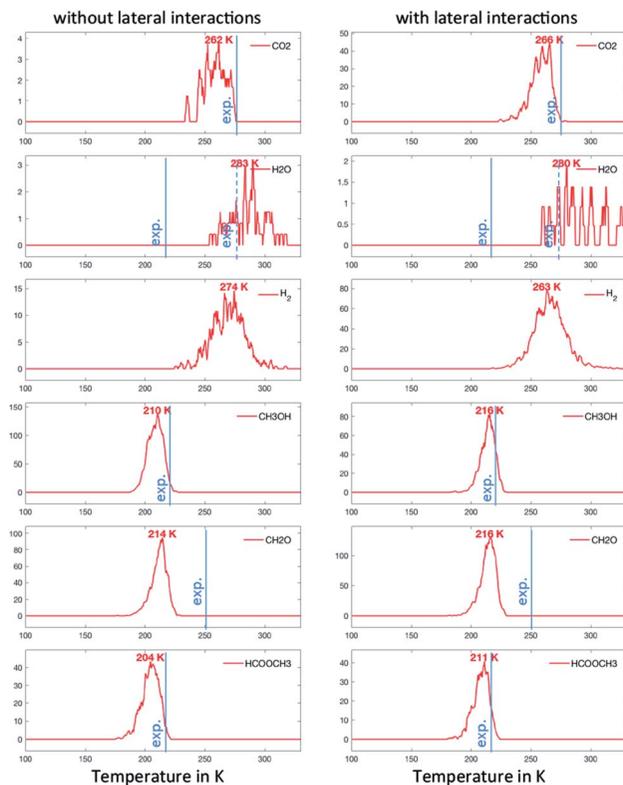
Fig. 5 TPO spectra of methanol on Au(111) for scenario #2. Temperature ramp is 10 K s^{-1}. The initial coverages are: 0.1 ML of CH_3O and 0.02 ML in O.

peak at 142 K corresponds to the C–H activation of CH_3O enabled by the presence of O, while the second one corresponds to the unassisted C–H activation of CH_3O (catalysed by the surface in the absence of a base). If the first peak were observed experimentally, it would probably appear around 185 K,[15] which is the normal desorption temperature of $HCOOCH_3$ (PBE-TS underestimates its adsorption energy, see Table 1). However, there is no such evidence. Moreover, water is also produced 50 K too early, as a direct consequence of the high reactivity of O with CH_3O, producing first OH and then H_2O. It is therefore likely that our initial configuration (CH_3O only with extra O) is too reactive when neglecting lateral interactions. When lateral interactions are included (Fig. 6, right panel), the low temperature water peak is shifted to higher temperatures and now matches the experimental data. More importantly, $HCOOCH_3$ now desorbs in one peak, correcting the main deviation to experiments seen in the 3rd scenario without lateral interactions (Fig. 6, compare left and right panels). These two observations can be attributed to the increase of the overall activation energy of O + $CH_3O \rightarrow$ OH + CH_2O from $\Delta^{\ddagger}E_{fwd} = 0.43$ eV to $\overline{\Delta^{\ddagger}E_{fwd}} = 0.56$ eV when including the repulsive interaction $IE_R = 0.13$ eV.

The last major deviation compared to the experimental TPO spectra is in the desorption of CH_2O. Experimentally the peak is very broad, starting at about 180 K
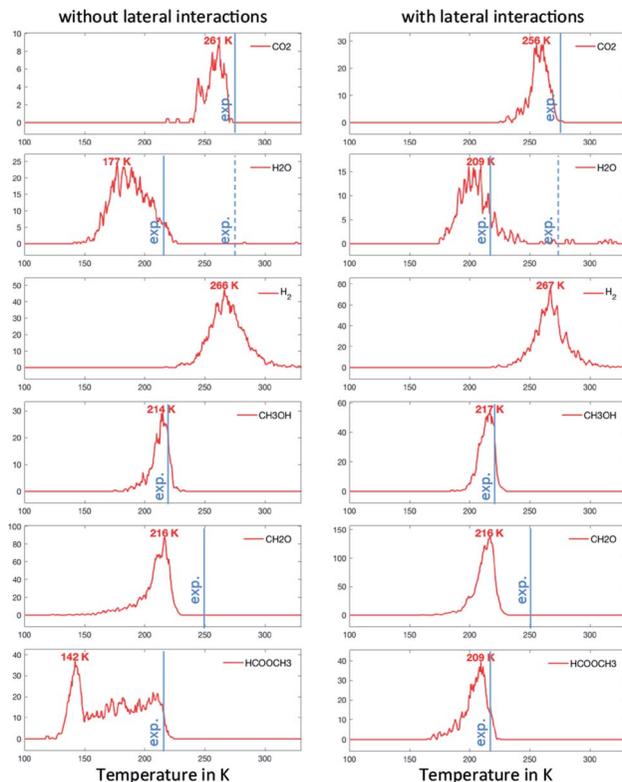
Fig. 6 TPO spectra of methanol on Au(111) for scenario #3. Temperature ramp is 10 K s^{-1}. The initial coverages are: 0.1 ML of CH_3O and 0.02 ML in O.

and expanding to 400 K.[15] This very likely results from a strong attractive interaction with water (−0.25 eV, see R12 in Table 2), which has not been included in our models. Other interactions might play a key role at low temperatures. As shown in Table 2, the lateral interactions of CH_3OH with O and OH (−0.24 and −0.26 eV respectively) and H_2O with O (−0.21 eV) are also strong and dominate over the reaction energies. It would therefore be no surprise that the oxygen atoms surrounded by water molecules would be less reactive than the bare oxygen atoms considered in our simulations. A better description of the initial complex equilibrium is therefore required to fully address the chemistry of the surface at very low temperatures, which is part of future work. Nevertheless, it is already remarkable that a DFT-parametrised model (involving no fitting to experimental data) gives us this amount of insight on such a complex system.

Conclusions

The present work adopts a multi-scale approach in the modelling of the TPO of methanol on O-precovered Au(111). Using DFT we have investigated the different elementary steps possible for the formation/cleavage of O–H and C–H bonds as well as different coupling reactions between electrophiles and nucleophiles. We

have shown that the presence of O lowers the activation energies of the C–H cleavages involved in the coupling pathway, but does not affect those of the over-oxidation route. We then built three different kinetic models, progressively incorporating complexity by adding relevant elementary steps (intrinsic reactivity of CH_3O, role of O to form CO_2 and role of O in C–H activations) and lateral interactions. These models reproduce the salient features of the TPO spectra, in particular, the desorption temperatures of CO_2 and the coupling product (methyl formate), as well as the water desorption when excess O is included in the initial state. Still though, deviations from the experimental observations (for example the width of the peaks) suggest that the initial state of the systems should be studied more thoroughly to explain the chemical equilibrium between the different species, as well as how they interact with each other in a tightly connected network of adsorbates. This understanding is of great importance considering that gold is also a prominent catalyst for alcohol oxidation in condensed phases, such as basic liquid water.[9] This however remains challenging[58] as it requires a high number of DFT calculations in order to get enough data to describe the interactions between the different adsorbates (O, OH, H_2O, CH_3O and CH_3OH) properly.

Conflicts of interest

There are no conflicts to declare.

Acknowledgements

References

1 H. Tohma and Y. Kita, *Adv. Synth. Catal.*, 2004, **346**(23), 111–124.

2 D. Morton and D. J. Cole-Hamilton, *J. Chem. Soc., Chem. Commun.*, 1988, **17**, 1154–1156.

3 N. Sieffert, R. Réocreux, P. Lorusso, D. J. Cole-Hamilton and M. Bühl, *Chem.–Eur. J.*, 2014, **20**, 4141–4155.

4 J. Clayden, N. Greeves and P. D. Wothers, *Organic Chemistry*, Oxford Uni., 2012, DOI: 10.1007/s00897010513a.

5 S. E. Davis, M. S. Ide and R. J. Davis, *Green Chem.*, 2013, **15**(1), 17–45.

6 M. M. Montemore, M. A. Van Spronsen, R. J. Madix and C. M. Friend, *Chem. Rev.*, 2018, **118**(5), 2816–2862.

7 A. P. Markusse, B. F. M. Kuster, D. C. Koningsberger and G. B. Marin, *Catal. Lett.*, 1998, **55**(3–4), 141–145.

8 M. S. Ide, D. D. Falcone and R. J. Davis, *J. Catal.*, 2014, **311**, 295–305.

9 Q. Gu, P. Sautet and C. Michel, *ACS Catal.*, 2018, **8**(12), 11716–11721.

10 A. Wittstock, V. Zielasek, J. Biener, C. M. Friend and M. Bäumer, *Science*, 2010, **327**, 319–322.

11 R. J. Madix, *Science*, 1986, **233**(4769), 1159–1166.

12 D. A. Outka and R. J. Madix, *Surf. Sci.*, 1987, **179**, 361–376.

13 D. A. Outka and R. J. Madix, *J. Am. Chem. Soc.*, 1987, **109**(6), 1708–1714.

14 J. Gong, D. W. Flaherty, R. A. Ojifinni, J. M. White and C. B. Mullins, *J. Phys. Chem. C*, 2008, **112**(14), 5501–5509.

15 B. Xu, X. Liu, J. Haubrich, R. J. Madix and C. M. Friend, *Angew. Chem., Int. Ed.*, 2009, **48**(23), 4206–4209.

16 B. Xu and C. M. Friend, *Faraday Discuss.*, 2011, **152**, 307–320.

17 B. Xu, R. J. Madix and C. M. Friend, *J. Am. Chem. Soc.*, 2010, **132**(46), 16571–16580.

18 J. Gong and C. B. Mullins, *J. Am. Chem. Soc.*, 2008, **130**(49), 16458–16459.

19 G. M. Mullen, L. Zhang, E. J. Evans, T. Yan, G. Henkelman and C. B. Mullins, *Phys. Chem. Chem. Phys.*, 2015, **17**(6), 4730–4738.

20 B. Xu, R. J. Madix and C. M. Friend, *Acc. Chem. Res.*, 2014, **47**(3), 761–772.

21 B. Xu, C. M. Friend and R. J. Madix, *Faraday Discuss.*, 2011, **152**, 241–252.

22 K. M. Kosuda, A. Wittstock, C. M. Friend and M. Bäumer, *Angew. Chem., Int. Ed.*, 2012, **51**(7), 1698–1701.

23 M. L. Personick, B. Zugic, M. M. Biener, J. Biener, R. J. Madix and C. M. Friend, *ACS Catal.*, 2015, **5**(7), 4237–4241.

24 C. Reece, M. Luneau and R. J. Madix, *ACS Catal.*, 2019, **9**(5), 4477–4487.

25 C. Reece, E. A. Redekop, S. Karakalos, C. M. Friend and R. J. Madix, *Nat. Catal.*, 2018, **1**(11), 852–859.

26 B. Xu, J. Haubrich, T. A. Baker, E. Kaxiras and C. M. Friend, *J. Phys. Chem. C*, 2011, **115**(9), 3703–3708.

27 S. Liu, P. Jin, D. Zhang, C. Hao and X. Yang, *Appl. Surf. Sci.*, 2013, **265**, 443–451.

28 L. Wang, C. He, W. Zhang, Z. Li and J. Yang, *J. Phys. Chem. C*, 2014, **118**(31), 17511–17520.

29 F. Cheenicode Kabeer, W. Chen, R. J. Madix, C. M. Friend and A. Tkatchenko, *J. Phys. Chem. C*, 2017, **121**(50), 27905–27914.

30 S. Kozuch and J. M. L. Martin, *ChemPhysChem*, 2011, **12**(8), 1413–1418.

31 S. Kozuch and S. Shaik, *Acc. Chem. Res.*, 2011, **44**(2), 101–110.

32 A. M. Ruppert, M. Jędrzejczyk, N. Potrzebowska, K. Kaźmierczak, M. Brzezińska, O. Sneka-Płatek, P. Sautet, N. Keller, C. Michel and J. Grams, *Catal. Sci. Technol.*, 2018, **8**(17), 4318–4331.

33 R. Réocreux, C. A. Ould Hamou, C. Michel, J. B. Giorgi and P. Sautet, *ACS Catal.*, 2016, **6**, 8166–8178.

34 M. Salciccioli, M. Stamatakis, S. Caratzoulas and D. G. Vlachos, *Chem. Eng. Sci.*, 2011, **66**, 4319–4355.

35 M. Stamatakis and D. G. Vlachos, *ACS Catal.*, 2012, **2**(12), 2648–2663.

36 M. K. Sabbe, M. F. Reyniers and K. Reuter, *Catal. Sci. Technol.*, 2012, **2**(10), 2010–2024.

37 M. Andersen, C. Panosetti and K. Reuter, *Front. Chem.*, 2019, **7**, 1–24.

38 G. Kresse and J. Hafner, *Phys. Rev. B: Condens. Matter Mater. Phys.*, 1993, **47**, 558–561.

39 G. Kresse and J. Furthmüller, *Comput. Mater. Sci.*, 1996, **6**, 15–50.

40 G. Kresse and J. Furthmüller, *Phys. Rev. B: Condens. Matter Mater. Phys.*, 1996, **54**, 11169–11186.

41 V. G. Ruiz, W. Liu, E. Zojer, M. Scheffler and A. Tkatchenko, *Phys. Rev. Lett.*, 2012, 146103.

42 G. Kresse and D. Joubert, *Phys. Rev. B: Condens. Matter Mater. Phys.*, 1999, **59**, 1758–1775.

43 H. J. Monkhorst and J. D. Pack, *Phys. Rev. B: Solid State*, 1976, **13**, 5188–5192.

44 G. Henkelman, B. P. Uberuaga and H. Jónsson, *J. Chem. Phys.*, 2000, **113**, 9901.

45 D. Sheppard, R. Terrell and G. Henkelman, *J. Chem. Phys.*, 2008, **128**, 134106.

46 G. Henkelman and H. Jónsson, *J. Chem. Phys.*, 1999, **111**, 7010.

47 A. Heyden, A. T. Bell and F. J. Keil, *J. Chem. Phys.*, 2005, **123**, 224101.

48 M. Stamatakis and D. G. Vlachos, *J. Chem. Phys.*, 2011, **134**(21), 214115.

49 J. Nielsen, M. D'Avezac, J. Hetherington and M. Stamatakis, *J. Chem. Phys.*, 2013, **139**(22), 224706.

50 R. Réocreux, C. Michel, P. Fleurat-Lessard, P. Sautet and S. N. Steinmann, *J. Phys. Chem. C*, 2019, **123**(47), 28828–28835.

51 B. C. Krüger, G. B. Park, S. Meyer, R. J. V. Wagner, A. M. Wodtke and T. Schäfer, *Phys. Chem. Chem. Phys.*, 2017, **19**, 19896–19903.

52 M. T. Darby, R. Réocreux, E. C. H. Sykes, A. Michaelides and M. Stamatakis, *ACS Catal.*, 2018, **8**(6), 5038–5050.

53 M. Pan, D. W. Flaherty and C. B. Mullins, *J. Phys. Chem. Lett.*, 2011, **2**(12), 1363–1367.

54 G. Kyriakou, E. R. M. Davidson, G. Peng, L. T. Roling, S. Singh, M. B. Boucher, M. D. Marcinkowski, M. Mavrikakis, A. Michaelides and E. C. H. Sykes, *ACS Nano*, 2014, **8**(5), 4827–4835.

55 J. J. Sims, C. A. Ould Hamou, R. Réocreux, C. Michel and J. B. Giorgi, *J. Phys. Chem. C*, 2018, **122**(35), 20279–20288.

56 S. N. Steinmann, C. Michel, R. Schwiedernoch, J.-S. Filhol and P. Sautet, *ChemPhysChem*, 2015, **16**, 2307–2311.

57 R. G. Quiller, T. A. Baker, X. Deng, M. E. Colling, B. K. Min and C. M. Friend, *J. Chem. Phys.*, 2008, **129**(6), 064702.

58 R. Réocreux and C. Michel, *Current Opinion in Green and Sustainable Chemistry*, 2018, **10**, 51–59.